



Simultaneous thermometry and velocimetry for a shock tunnel using homodyne and heterodyne detection

Tobias Sander¹ · Jens Weber¹ · Christian Mundt¹

Received: 3 March 2022 / Accepted: 11 May 2022 / Published online: 23 July 2022
© The Author(s) 2022

Abstract

At our institute a piston-driven shock tunnel is operated to investigate structures of space transportation systems under reentry and propelled flight conditions. For temperature measurements in the nozzle reservoir under single-shot conditions, laser-induced thermal grating spectroscopy is used to date to measure the speed of sound of the test gas. The temperature then can be calculated from this data. The existing experimental setup has already been successfully used to measure flows up to an enthalpy of 2.1 MJ/kg. Since conducting the experiments is extremely time-consuming, it is desirable to extract as much data as possible from the test runs. To additionally measure the velocity of the test gas, the test setup was extended. Besides, extensive improvements have been implemented to increase the signal-to-noise ratio. As the experiments can be conducted much faster at the double-diaphragm shock tube of the institute without any restrictions on the informative value, the development of the heterodyne detection technique is carried out at this test facility. A series of 36 single-shot temperature and velocity measurements is presented for enthalpies of up to 1.0 MJ/kg. The averaged deviation between the measured values and the values calculated from the shock equations of all measurements related to the average of the calculated values is 2.0% for the Mach number, 0.9% for the velocity after the incident shock and 4.8% for the temperature after the incident shock.

List of symbols

Latin letters

a	Sound velocity m/s
u	Flow velocity, shock normal m/s
v_{flow}	Flow velocity, parallel to \mathbf{q} m/s
T	Temperature K
M	Mach number –
h	Specific enthalpy J/kg
p	Pressure Pa
R_s	Specific gas constant J/(kg K)
\mathbf{q}	Grating wave vector 1/m
I	Signal intensity W
U_{at}	Attenuator voltage V

Greek letters

Ω_a	Resonant (Brillouin) beat frequency Hz
Ω_0	Non-resonant signal beat frequency Hz
$\Omega_{1,2,3}$	Heterodyne signal beat frequencies Hz
ω_0	Probe beam frequency Hz

$\omega_{1,2,3}$	Signal beam frequencies Hz
$\Delta\omega_s$	Reference beam frequency shift Hz
Λ	Grating constant m
γ	Isentropic exponent –

Subscripts

LIGS	Laser-induced grating spectroscopy
SE	Shock equation

1 Introduction

For the experimental simulation of the reentry and propelled flight of space transportation systems, a piston-driven shock tunnel HELM (High Enthalpy Laboratory Munich) is in operation at the Institute of Thermodynamics at the Universität der Bundeswehr München [1, 2]. For a better characterization of the thermodynamic properties of the test gas in the nozzle during experiments and to obtain data for the numerical simulation of high-enthalpy flows, knowledge of the temperature within the nozzle reservoir and the flow velocity is required. Optical measurement techniques are well suited for measurements in high-enthalpy flows as they do not influence the flow and are not subject to mechanical and thermal limits like probes. Further challenges for the measurement technique are the extremely high temperature

✉ Tobias Sander
tobias.sander@unibw.de

¹ Fakultät für Luft- und Raumfahrttechnik, Institut für Thermodynamik, Universität der Bundeswehr München, Werner-Heisenberg-Weg 39, 85577 Neubiberg, Germany

and pressure as well as the very short measurement time in the nozzle reservoir of shock tunnels, which can be overcome by optical measurement techniques. Homodyne laser-induced thermal grating spectroscopy (LITGS, also called resonant LIGS or resonant LITA) needs no seeding particles and offers the possibility of temperature measurements with a high temporal resolution [3–7] under single-shot conditions. In addition, only a small optical access is required for this method, which is particularly advantageous for measurements under high temperatures and pressures. It is important to note that the signal strength in laser-induced grating spectroscopy increases with increasing pressure and decreases with increasing temperature.

$$I \propto p^x T^y. \quad (1)$$

In the literature, different values can be found for x and y , which also differ between the procedures electrostrictive (LIEGS, also called non-resonant LIGS or non-resonant LITA) and LITGS. In the work of Förster et al. [7], the value 2 is given for x and -3.4 for y for LIEGS. Schlamp et al. [8] report, deviating from this, $y = -3$ (fluid at rest) or $y = -4.25$ (flowing fluid). Danehy et al. [9] specify for $x = 2$ and for $y = -3$. For LITGS they mention for $x = 4$ and $y = -6$ (low density) and for $x = -2$ and $y = -0.6$ (high density), respectively. However, it should be noted that only pressures up to 0.13 MPa were studied and it is suspected that the downward trend of x should decrease at much higher pressures.

Laser-induced thermal grating spectroscopy can also be used to determine species concentrations in addition to temperature measurement. For this purpose, Schlamp et al. [10] studied iodine vapor as resonantly excitable species with different concentrations in a non-resonant N_2 environment at the excitation wavelength used. To determine the concentration of iodine, they used the amplitude ratio of thermal and electrostrictive signal after a calibration procedure at several known concentration ratios. They assume that the electrostrictive signal component of the excited species is negligible. The detection limit of this species depends on the amplitude ratio of both signal components and is 10 to 130 ppm in this study. The authors achieve an uncertainty of 5% for the concentration measurement and of 0.35% for the sound velocity measurement, respectively.

As early as 1998, Cummings [11] proposes to use heterodyne laser-induced grating spectroscopy for velocity measurements in gas flows. For this purpose, the beat of a Doppler frequency-shifted signal beam can be evaluated against a reference beam.

Walker et al. [12] present data on velocity measurements in gas flows ranging from 30 to 180 m/s using laser-induced thermal grating spectroscopy. In the setup used, the laser-induced grating scatters only a portion of the photons at the

Bragg angle. The rest of the probe beam hits a mirror and reads out the laser-induced grating in the opposite direction to the incident beam. This results in two signal beams that are frequency-shifted in opposite directions but with double amount. The two beams are passed through a Fabry-Perot etalon to produce separate fringe patterns on a CCD camera. The relative displacement of the fringes yields the frequency difference of the two signals, which is twice the Doppler shift. By fitting these fringes to theoretical ones the frequency shifts were determined. They report a single-shot measurement precision of $\pm 8\%$, which improved with increasing flow velocity and therefore emphasize that the method presented is best suited for flows that have higher velocities than those studied here.

Kozlov et al. [13] use LIEGS to measure temperature fields (up to 600 K) and flow velocities (10 to 160 m/s) in a steady flow. The experimental setup is similar to that of Walker et al. [12] i.e., no reference beam is used here either. Instead, after reflection at a mirror, the probe beam passes through the measurement volume a second time and, due to the change in direction, now experiences the Doppler shift with a sign opposite to that of the first beam. The superposition of both signal beams leads to a beat frequency, which is evaluated to measure the velocity. One of the two signal beams is used to measure the temperature. The authors propose to use the time history of the LIGS signal to characterize the flow turbulence. They note that for single-shot measurements, it seems easier to perform signal evaluation in the frequency domain using the Fast Fourier transform, as applied in the present work. In a later study, the author describes in [14] the measurement of speed of sound, thermal diffusivity and bulk viscosity by means of LITGS, emphasizing the versatility of this measurement technique and the possibility to measure several quantities simultaneously.

Schlamp et al. [15] use heterodyne laser-induced thermal grating spectroscopy to simultaneously measure sound speed and flow velocity up to a Mach number of 0.1 in single-shot mode with NO_2 seeded air. They each report an uncertainty of 0.5%. In contrast to [12], a reference beam is used here that does not pass through the measurement volume and thus does not experience a Doppler shift. The use of an optical chopper to cut laser pulses with a duration of 20 μs from the continuous reference beam should be emphasized. This achieves an extension of the linear working range of the photomultiplier. However, a disadvantage here is that the exposure of the detector cannot be synchronized exactly with the arrival of the signal beam, when conducting externally triggered single-shot experiments. Schlamp et al. also propose the use of a Bragg cell in order to shift the frequency of the reference beam and thus to be able to separate the frequencies to be measured from the low-frequency noise. In the present work, a frequency shifter is used for this purpose

in order to reduce heterodyne signal ambiguity. However, the control of this component is coupled to the Q-switch of the pump laser in order to expose the photomultiplier of the heterodyne channel only as short as possible during the lifetime of the grating and thus to prevent overexposure as far as possible.

In another study [16], Schlamp et al. describe homodyne velocity measurement based on intentional misalignment of the reference beam relative to the crossed pump beams. The evaluation is done by fitting the measured signals with theoretically modeled ones, where these include the effects of flow velocity and jet displacement as parameters. The advantage here is a much simpler measurement setup compared to heterodyne detection. In addition, the aforementioned problem of frequency separation of heterodyne and homodyne signals is eliminated. The authors investigate subsonic and supersonic flows up to a Mach number of 2 of NO₂ seeded air and report a satisfactory agreement between theory and experiment.

In contrast to Walker et al. [12] and Kozlov et al. [13], Hemmerling et al. [17] only use one signal beam in combination with a reference beam in their heterodyne LIEGS setup. The latter is shifted in frequency by a Bragg cell and superimposed with the signal beam in an optical fiber. Section 2 revisits the difference between the two concepts and describes the impact on the practical implementation of both setups. Both variants of laser-induced grating spectroscopy (frequency shift and optical fiber coupling) are used in the present study, but in contrast to [17] in the form of LITGS. The reasons for this will be discussed in detail. The authors measure in a cold N₂ jet of a sub-scaled rocket nozzle at stagnation pressures of 10 bar to validate CFD calculations. They achieve standard deviations of 16.4 m/s (mean velocity: -4.5 m/s) and 11.6 m/s (mean velocity: -9.2 m/s), respectively.

Neracher, one of the authors of [17] describes in [18] the measurements by heterodyne LIEGS in a similar setup. In a free jet, flow velocities of up to 60 m/s with a standard deviation of 1.5 to 2.5 m/s and temperatures up to 525 K with a standard deviation of 1–2% are measured. The authors of [18] use a frequency shift of the reference beam of 2.2 MHz, those of [17] a comparable shift of 3.5 MHz. In heterodyne detection of electrostrictive gratings, the frequencies used to measure the sound velocity of the medium Ω_0 and those used to measure the expected flow velocity are relatively far apart. In heterodyne LITGS, on the other hand, the Brillouin frequency Ω_a and the frequencies shifted by the flow velocity are close to each other. Therefore, a larger frequency shift of about 65 MHz is chosen in this study so that the frequencies are farther apart in the image domain and correspondingly easier to identify.

A more recent work on measurements with laser-induced gratings can be found in Förster [7]. The experimental setup

used is basically based on those of Schlamp et al. [16] and Hemmerling et al. [17]. As in [17] and [18], an electrostrictive grating is detected. However, optical fibers are used for mixing signal and reference beams as well as for guiding the beams to the detector. Thus, it is possible to detect both the homodyne and heterodyne signals simultaneously. Single-shot measurements of temperature, sound velocity and flow velocity are performed on a shock tube behind the incident as well as the reflected shock at test gas temperatures up to 1000 K and pressures up to 43 bar. The single-shot standard deviations for Mach number, sound velocity and temperature are 1%, 1.7% and 3.4%, respectively. In the present work, optical fibers were also used for mixing the beams and simultaneous detection of homodyne and heterodyne signal by two independent detectors. This allows a plausibility check of the measured values and additionally, in case of weakly pronounced beat on the heterodyne channel, at least the determination of the sound velocity of the test gas. However, unlike [7], photomultipliers were used here instead of photodiodes, the former having greater sensitivity.

In another paper by this group (Baab et al. [19]), LIEGS is used to measure the local speed of sound in the farfield of an underexpanded jet (n-hexane in quiescent N₂). The authors present radially resolved speed of sound profiles at different axial positions and at different injection temperatures. Using an adiabatic mixing model, mixture composition and temperature are extracted from the experimental data. This shows that laser-induced grating spectroscopy can be used to measure different physical quantities simultaneously.

2 Theoretical considerations

The physical background to the formation of laser-induced gratings and their readout are described in various papers [11–22]. In the following section, the frequencies resulting from the superposition of Doppler-shifted laser beams are discussed in detail. These shifts are caused by the thermos and phonons induced in the grating, by the flow velocity prevailing in the measurement volume and by a frequency shift of the readout beam generated by an acousto-optic modulator used in this work to uniquely identify the measurable frequencies. Please note that in this study all specified frequencies Ω and ω are treated as ordinary frequencies not as angular frequencies.

Two crossing pump laser beams with the wave vectors \mathbf{k}_1 and \mathbf{k}_2 generate an interference grid with the grating constant Λ and the wave vector \mathbf{q} . The value of the grating vector q is expressed by

$$q = \frac{2\pi}{\Lambda}. \quad (2)$$

If the pump beams create a thermal grating, which can be explained by the superposition of a static thermal and two phonons propagating in opposite directions with the speed of sound [20], diffraction of the probe beam occurs at the Brillouin frequency Ω_a , resulting in an oscillating signal beam. Ω_a corresponds to the frequency of the acoustic wave and is determined by the fringe spacing of the grating and the speed of sound a of the medium.

$$\Omega_a = \frac{a}{\Lambda} \quad (3)$$

In the case of an electrostrictive grating resulting from two phonons only counterpropagating with the speed of sound [20], the modulation of the density grating occurs at twice the Brillouin frequency $\Omega_0 = 2\Omega_a$ corresponding to the velocity of the phonons relative to each other. Which of the two types of gratings is formed depends on the composition of the test gas as well as the frequency of the pump beam photons. For the formation of a thermal grating, the presence of an absorbing species in the test gas as well as the appropriate excitation frequency of the pump beam photons are necessary conditions.

The grating constant of the adjusted optical setup or the value of the grating vector is calculated a priori using Eq. 3 after measuring the frequency $2\Omega_a$ (electrostrictive or non-resonant grating) or Ω_a (thermal or resonant grating) at a known temperature i.e. at a known sound velocity of the test gas. For the measurements, Eq. 3 is used to determine the sound velocity. For non-reacting gases the temperature T then can be calculated using the expression:

$$T = \frac{a^2}{\gamma(T)R_s(T)} \quad (4)$$

with the isentropic exponent γ and the specific gas constant R_s . At our institute a homodyne LITGS measurement setup was developed [23] and its operability was proven in a conventional shock tube and at HELM [3, 24–28].

In order to simultaneously measure the temperature and the velocity of the test gas during the single-shot experiment, heterodyne laser-induced grating spectroscopy can be applied. The formation and the absolute value of the beat frequencies are first described on the basis of the superposition of the Doppler-shifted light beams using an electrostrictive grating. Subsequently, the differences that exist with a thermal grating, which will be used for the application at HELM, will be discussed.

In a quiescent medium, the frequency of the diffracted probe beam ω_0 is Doppler-shifted by the frequency of the acoustic waves travelling with the speed of sound a in opposite directions and leading to the two frequencies ω_1 and ω_2 :

$$\omega_{1,2} = \omega_0 \pm \frac{a}{\Lambda} = \omega_0 \pm \Omega_a. \quad (5)$$

The interference of these frequencies causes an oscillating signal with the beat frequency Ω_0 , which can be described as:

$$\Omega_0 = \omega_1 - \omega_2 = 2\Omega_a. \quad (6)$$

If the signal beam of a test gas with flow velocity $v_{flow} = 0$ is mixed with a reference beam i.e. a laser beam with the same frequency as the probe beam ω_0 , an additional peak appears in the spectrum at the beat frequency Ω_a corresponding to the absolute velocity a of the wave packages, Eq. 7.

$$\Omega_a = |\omega_0 - \omega_{1,2}| \quad (7)$$

If the test gas has a velocity $v_{flow} \neq 0$ parallel to \mathbf{q} at the time of measurement, an additional Doppler-shift occurs:

$$\omega_{1,2} = \omega_0 - \frac{v_{flow}}{\Lambda} \pm \Omega_a. \quad (8)$$

In the homodyne case, the signal beam interference of ω_1 and ω_2 (i.e. the relative velocity of the two wave packages) is not influenced by the flow velocity and therefore the power spectrum still only shows a peak at the beat frequency Ω_0 , Eq. 6. In the heterodyne case, the signal beam is mixed with a reference beam producing beat frequencies corresponding to the frequency differences between the reference beam and the signal beam. These beat frequencies can be written as:

$$\Omega_2 = \omega_0 - \omega_2 = \frac{v_{flow}}{\Lambda} + \Omega_a \quad (9)$$

$$\Omega_1 = \omega_0 - \omega_1 = \frac{v_{flow}}{\Lambda} - \Omega_a \quad (10)$$

and are appearing in the power spectrum as two additional peaks. Equation 10 shows that Ω_1 becomes negative for subsonic conditions and thus appears phase-shifted in the frequency spectrum by π . The flow velocity then can be calculated using the following expression, which is valid for subsonic and supersonic conditions:

$$v_{flow} = \frac{\Lambda}{2}(\Omega_2 + \Omega_1). \quad (11)$$

As mentioned above, the frequency Ω_0 (twice the Brillouin frequency Ω_a) primarily occurs if an electrostrictive grating is formed. While in the case of a thermal grating the modulation of the probe beam occurs with the Brillouin frequency [20]. Here, the power spectrum may have a signal at the Brillouin frequency that could come from either homodyne detection or heterodyne detection in the case of $v_{flow} = 0$. Therefore care has to be taken evaluating the measurement signal.

In order to overcome this challenge, a frequency shifter was integrated in the beam path of the reference beam shifting its frequency ω_0 by $\Delta\omega_s$ in order to be able to doubtlessly distinguish between the above mentioned signals. The frequencies Ω_1 and Ω_2 can then be expressed by:

$$\Omega_{2,1} = (\omega_0 + \Delta\omega_s) - \omega_{2,1} = \Delta\omega_s + \left(\frac{v_{flow}}{\Lambda} \pm \Omega_a\right). \quad (12)$$

In the case of a thermal grating, diffraction of the probe beam at the static thermon results in an additional frequency ω_3 , which causes a Doppler shift corresponding to the flow velocity:

$$\omega_3 = \omega_0 - \frac{v_{flow}}{\Lambda}. \quad (13)$$

The frequency Ω_3 appears as a beat frequency resulting from the interference of the frequency-shifted reference beam with the signal beam component with frequency ω_3 :

$$\Omega_3 = (\omega_0 + \Delta\omega_s) - \omega_3 = \Delta\omega_s + \frac{v_{flow}}{\Lambda}. \quad (14)$$

Using Eq. 14, the flow velocity v_{flow} can be calculated by identifying Ω_3 in the frequency spectrum if the values for the grating constant Λ and the shift of the reference beam $\Delta\omega_s$ are known. The frequencies expected for a given configuration are summarized in Table 1. The terms resonant/non-resonant refer to the mechanism for inducing a thermal/electrostrictive grating or LITGS/LIEGS, respectively. All frequencies mentioned in this section depend on the configuration of the measurement setup.

As announced in Sect. 1, the following section will look at the difference in the configurations of Walker et al. [12] and Kozlov et al. [13] versus that of Hemmerling et al. [17] and their significance for practical implementation. When using an acousto-optical frequency shifter, the frequency of the reference beam is shifted by a fixed amount $\Delta\omega_s$, which depends on the settings on the control unit. This method is used both in this paper and by Hemmerling [17]. In contrast, a variable shift of the reference beam $\Delta\omega_{s,variable}$ occurs when the grating is read out from two opposite sides:

$$\Delta\omega_{s,variable} = \frac{v_{flow}}{\Lambda}. \quad (15)$$

This results in two oppositely frequency-shifted signal beams depending on the flow velocity and the grating constant. Here, the portion of the signal resulting from diffraction at the front of the grating is defined as the reference beam. The advantage of fixed frequency shifting is the reduced beam alignment effort and the fact that there is no need to ensure symmetry between the readout beams. Furthermore, the alignment process to obtain a homodyne LIGS signal is decoupled from the process of frequency shifting the reference beam. In principle, therefore, it can be concluded that the use of a fixed frequency shift is the more robust method, although the complexity of the setup increases due to the use of an additional component.

The presented approach allows to classify configurations that do not use an explicit reference beam but a variably shifted reference beam, such as those of Walker [12] and Kozlov [13], and to apply the equations for the frequencies of the signal spectrum (Table 1) to them. This approach makes this table a universally useful summary for all LIGS configurations considered in this study, regardless of whether the reference beam is shifted by a fixed or variable amount. The mentioned shift configurations are summarized in Table 2 and apply to the beat frequency equations in this section. The authors emphasize that all discussed variants of the laser-induced grating spectroscopy can be realized with the experimental setup presented here. Nevertheless, it should be noted that resonant excitation appears to be more suitable than non-resonant excitation for the planned application at HELM under high-enthalpy conditions [9]. Therefore, the focus of this work is on the development of a measurement method based on resonant excitation.

As mentioned above, the formation of a thermal grating requires an absorbing species in the test gas as well as the appropriate excitation frequency of the pump beam photons. The absorbing species (e.g. NO₂) is either formed during experiments under high-enthalpy conditions or can be added before the experiment (seeding). In this work, the seeding concentration was set between 1670 and 20000 ppm depending on the experimental condition. However, lower concentrations are also sufficient for an evaluable signal. For example, seeding concentrations between 235 and 500 ppm were used for measurements at HELM at stagnation enthalpies

Table 1 Classification of LIGS in terms of configuration and occurring signal frequencies

Configuration	Signal frequencies	Reference beam frequency
C1 Non-resonant homodyne	Ω_0	–
C2 Non-resonant heterodyne	$\Omega_0, \Omega_1, \Omega_2$	$\omega_0 + \Delta\omega_s$
C3 Resonant homodyne	Ω_a, Ω_0	–
C4 Resonant heterodyne	$\Omega_a, \Omega_0, \Omega_1, \Omega_2, \Omega_3$	$\omega_0 + \Delta\omega_s$

Table 2 Frequency shift configurations of reference beam

Shift configuration	Frequency shift $\Delta\omega_s$
No shift	$\Delta\omega_s = 0$
Fixed shift	$\Delta\omega_s = \text{constant}$
Variable shift	$\Delta\omega_s = v_{flow}/\Lambda$

between 1.2 and 2.1 MJ/kg for an evaluable signal-to-noise ratio [28]. Only under moderate conditions, such as those present in the cases studied here, seeding of the test gas may be necessary to achieve a high signal-to-noise ratio (SNR), while under higher pressures and temperatures formation of a sufficient amount of NO_2 is expected.

Moreover, in LITGS, in the presence of an excitable species, the pulse energy of the pump laser can be chosen to be much lower than in LIEGS, which has a positive effect on the lifetime of the quartz windows and also generates less stray light that would degrade the signal quality. However, as pure NO_2 is a toxic and highly corrosive substance, it is unsuitable for seeding purposes. Therefore, in this work, a commercial NO-N_2 test gas is mixed with air to produce a sufficient concentration of the absorbing species NO_2 by chemical reaction. The absorption system of one single electronic transition of NO_2 extends from the ultraviolet spectrum ($\text{B}^2\text{B}_2 - \text{X}^2\text{A}_1$) to the visible ($\text{A}^2\text{B}_1 - \text{X}^2\text{A}_1$) with a global maximum at 435 nm [29, 30]. At the emission wavelength of the used pump laser of 532 nm (see Sect. 3.1 for details) the absorption is sufficiently high. In own former works [31] the formation of NO_2 after seeding the test gas with dry air and its absorption behavior was investigated with absorption measurements in a test cell. It is assumed that the isentropic exponent γ of the test gas does not change due to seeding, since the seeding components NO and N_2 are diatomic molecules, like the main components of dry air, N_2 and O_2 , and since the amount of NO_2 formed is small.

3 Experimental

3.1 Optical setup

In order to realize the heterodyne detection, the existing optical measurement setup for homodyne detection had to be extended by optical and electronic components, which are described in the following section. The test setup shown in Fig. 1 essentially is based on the above mentioned own former works.

It consists of a pulsed Nd:YAG laser (wavelength: 532 nm, maximum pulse energy: 200 mJ, pulse duration: 7 ns). The beam of this laser is split into two pump beams with equal pulse energy, which generate the interference grid. The probe beam used to read out this grid is provided by a continuous diode laser (wavelength: 488 nm, maximum power: 2 W). A small part (10%) of the readout beam can be separated by a beam splitter and adjusted symmetrically to the probe beam with respect to the optical axis of the lens. In this way it serves as the simulated signal beam and can be used for a first rough adjustment of the optical path to the detector.

For the single-shot experiments, a movable beam trap blocks this alignment beam and the beam splitter divides the beam into the probe (90%) and the reference beam (10%). While the former is directed into the measurement volume to read out the laser-induced grating, the latter is used to generate the heterodyne signal and is coupled into an optical fiber. Two beam paths are shown between the frequency-tunable acousto-optical modulator (wavelength of operation: 488 nm, frequency range: 60–100 MHz) and the coupler of the reference beam. Only when a predefined radio frequency (RF) tuning voltage is applied to the frequency shifter, the reference beam is guided via the coupler into the optical fiber, as the diffraction angle depends on the input voltage. In addition, the modulator shifts the frequency of the reference beam by $\Delta\omega_s$, which is also depending on the tuning voltage. For maximum strength of the superposition signal, the reference beam and the signal beam must have comparable intensity. However, since this is up to four orders of magnitude higher for the reference beam than for the signal beam [11], the electronic fiber-coupled optical attenuator is used to reduce the intensity of the reference beam in the optical fiber in response to a constant control voltage provided by the oscilloscope's waveform generator (G1). The optical transmission of the attenuator vs. the applied voltage is shown in Fig. 2. With increasing voltage from 0 to 5 V, the transmission is attenuated by 2.5 to 30 dB.

The right fiberoptic splitter splits the homodyne LIGS signal fed into the fiber via a coupler in a 50/50 ratio into two fiberoptic cables. The left fiberoptic mixer superimposes 50% of the homodyne LIGS signal and the reference beam in a ratio of 90/10 to form the heterodyne LIGS signal. The beat frequencies Ω_1 , Ω_2 and Ω_3 resulting from the Doppler-shift are detected by the photomultiplier (PMT) ps3 (heterodyne detection). The flow velocity of the test gas v_{flow} at the time of measurement can then be calculated using Eq. 14. The photomultiplier ps2 (homodyne detection) detects the other half of the signal. Another photomultiplier (ps1) is used for finding the LIGS signal and coupling it into the fiber, which is only required during initial alignment or adjustment of the optical setup. The respective voltage signals are recorded by an oscilloscope (bandwidth: 4 GHz, sampling rate: 20 Gsample/s). It should be mentioned that in the described detection scheme, the signal beam exiting the measurement volume is split into two halves, one for the homodyne and one for the heterodyne channel. Therefore, the detectable signal strength on each channel is halved accordingly.

Since the measurement time at the shock tube is in the range of a few milliseconds, very precise synchronization of the components of the measurement setup (i.e. laser and detector) is required to perform the measurements. In experimental operation, the triggering event of the measurement is the incident shock, which generates a voltage edge via a piezoelectric pressure sensor (sensitivity: 1.45 mV/kPa,

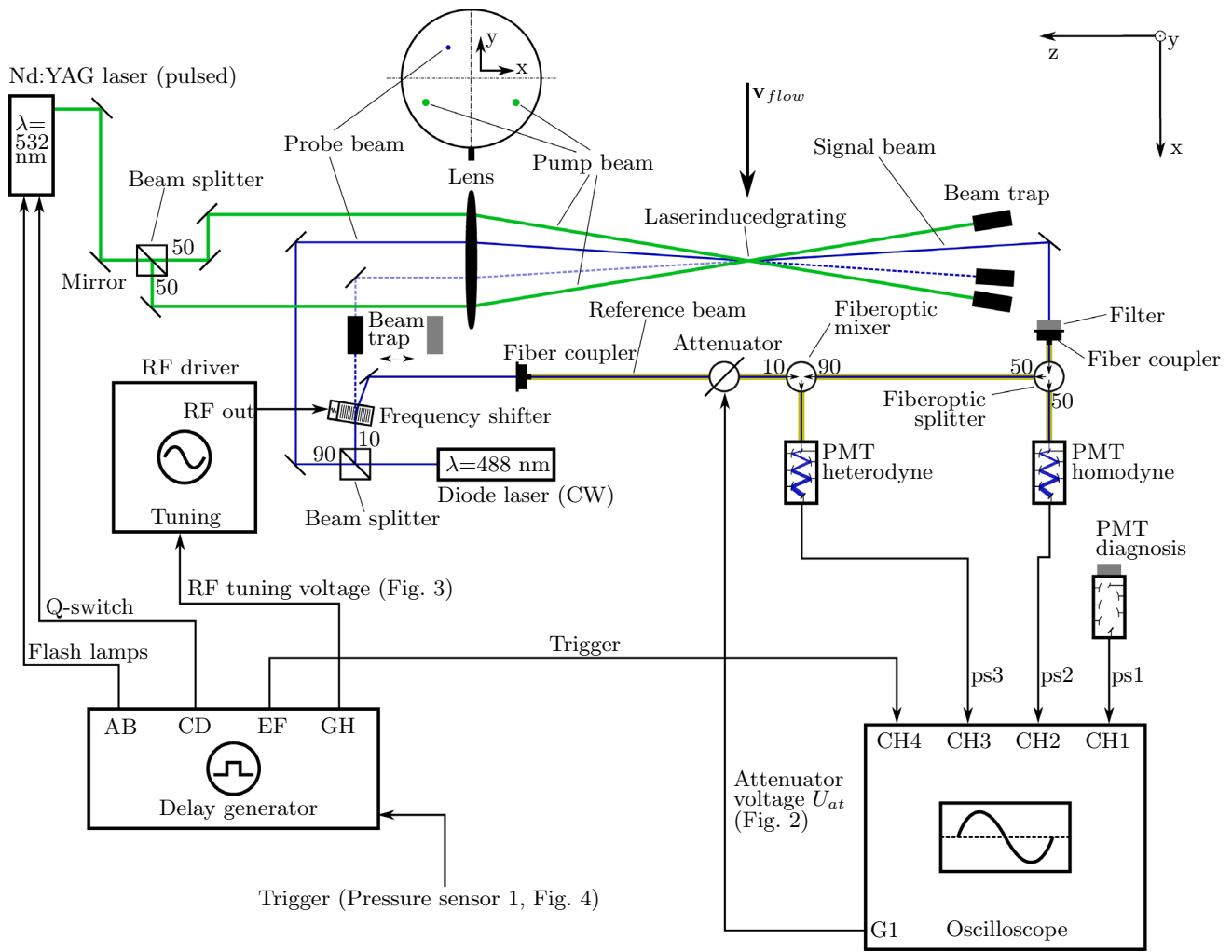


Fig. 1 Schematic of the optical setup for the resonant fixed shift homodyne and heterodyne detection

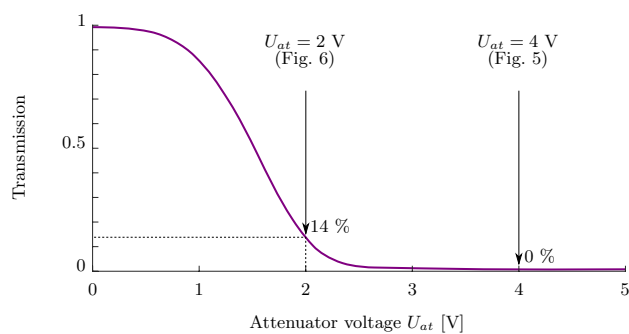


Fig. 2 Transmission of the attenuator vs. applied voltage

maximum pressure: 34.5 MPa) and downstream charge amplifier, which is fed as input to a delay generator. This component triggers the flash lamps and the Q-switch of the Nd:YAG laser via TTL pulses with very finely adjustable pulse duration and time delay relative to the input signal, as

well as the trigger signal for the oscilloscope, which records the trigger pulse of the delay generator in addition to the voltage signals of the photodetectors. The frequency shifter is also triggered by the delay generator with a duration of 5 μ s to avoid glare or damage to the detector from the intense reference beam. Figure 3 shows the signal recorded by the PMT ps3 (upper half) as a result of the TTL pulse (lower half). For this demonstration purpose, the power of the diode laser was set to a minimum value and the attenuation voltage to $U_{at} = 0$ V.

3.2 Test facility

The optical setup was used on a conventional double-diaphragm shock tube with a solid end and optical access which is very well suited for metrology development due to its easy handling and mechanical simplicity. The length of the driver section is 1.5 m, the length of the driven section is 8 m, the diameter of the shock tube is 100 mm. The shock tube can

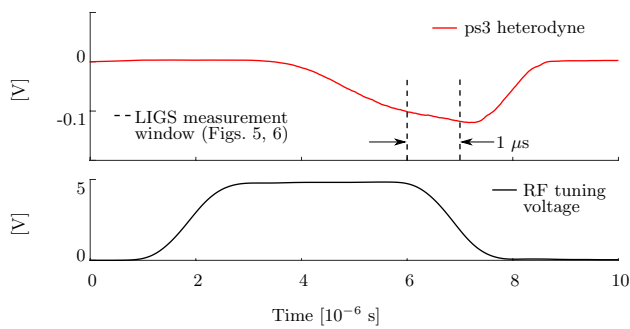


Fig. 3 Signal recorded by the PMT ps3 (upper half) and TTL pulse (lower half). Power of the diode laser minimal, attenuation voltage $U_{at} = 0$ V

be operated with a maximum driver pressure of 10 MPa and is divided into the three sections driver, double diaphragm chamber and shock tube.

The diaphragms open at a pressure difference defined by the depth of the milled groove and the diaphragm thickness. When filling the test rig, the double diaphragm chamber is now filled so that the pressure there is about half that in the driver. The pressure difference between the driver p_4 and the driven section p_1 can exceed the burst pressure of the diaphragms, since the pressure difference across each of the two diaphragms is below its burst pressure. Another element of the trigger mechanism is a vessel evacuated before the measurement which is connected to the double diaphragm chamber by a valve. When this is opened, the pressure in the double diaphragm chamber drops abruptly, causing the pressure difference between the driver and the double diaphragm chamber to exceed the burst pressure of the diaphragms, and the diaphragms both open abruptly. As a result, a shock moves through the driven part. Thus, the double diaphragm chamber ensures a defined opening of the diaphragms and is thus part of the release mechanism.

The velocity and Mach number of the incident shock were determined from the time interval between the resulting pressure jumps recorded by two pressure sensors placed at a distance of 20 mm and 70 mm from the solid end of the shock tube and the temperature of the test gas measured before the experiment. The pressure signals as well as the Q-switch output of the pump laser are recorded by an oscilloscope (bandwidth: 200 MHz, sampling rate: 1 Gsample/s). Thus, the pressure in the shock tube at the time of the measurement can be measured and used as a basis for the gas-dynamic calculation. In order to validate the data derived from the optical measurement, the temperature behind the shock, the post-shock Mach number and the flow velocity behind the shock were calculated using the shock equations for ideal gas. The optical access sits in the middle of the pressure gauges, thus 45 mm from the solid end. The fact that the Q-switch pulse is recorded together with

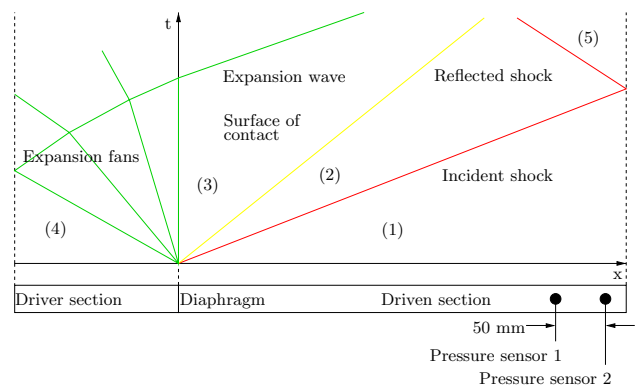


Fig. 4 x-t-diagram and schematic sketch of the shock tube

the pressure signals makes it possible to see whether the measurement took place before (state 2) or after (state 5) the reflected shock.

In Fig. 4 a general x-t-diagram which represents the flow conditions over time and a schematic sketch of the shock tube are illustrated. The driver pressure (state 4), and the shock tube pressure (state 1) are decisive for the charging state of the test bench. The double diaphragm chamber is shown in simplified form as one diaphragm. The incident shock compresses, heats and accelerates the test gas towards the solid end of the shock tube (state 2). The velocity in state 2 depends on the set pressure in the driven section, with a higher pressure p_1 causing a lower velocity u_2 . When the reflected shock passes through the medium again, it causes further compression and heating, as well as deceleration to the resting state (state 5).

4 Results and discussion

4.1 Effect of the frequency-shifted reference beam

As mentioned in Sect. 2, the aim of this work was the development of the heterodyne detection based on the thermal grating (resonant LIGS). Under the presence of an absorbing species (NO_2 in our case) the thermal grating will dominate over the electrostrictive one. However, the heterodyne signal of an unshifted reference beam under no-flow condition appears at the same frequency as the thermal signal (Ω_a) and cannot be differentiated from this (see Eq. 12, $v_{flow} = 0$, $\Delta\omega_s = 0$). Consequently, the strength of the heterodyne signal cannot be estimated. This means that it is not possible to set the correct voltage for an optimum signal on the attenuator before measurement in steady state, i.e. after filling the shock tube with a defined seeded gas mixture. To circumvent this problem, a frequency shifter was integrated into the experimental setup, which has already been described in Sect. 3.1. The frequency shift $\Delta\omega_s$ of the

reference beam achieved with this component allows the distinction between the homodyne and the heterodyne signal and thus an alignment of the corresponding intensities via the attenuator.

To illustrate the operation of the frequency shifter, in Fig. 5 both the signals (upper part, blue graph: homodyne, ps2, red graph: heterodyne, ps3) and their corresponding Fast Fourier Transform (lower part) are shown, which were measured at an attenuator voltage of 4 V and a RF tuning voltage at the frequency shifter of 5 V corresponding to a frequency shift of approx. 61.4 MHz. As mentioned in Sect. 3.1, the frequency shifter was operated with a pulse duration of 5 μ s to optimize the heterodyne signal. Due to the high attenuation voltage, only a very small fraction of the reference beam is transmitted (Fig. 2), so that it has no influence on the signal detected by the PMT ps3. Also with the Fast Fourier Transform, only the frequencies Ω_a and $\Omega_0 = 2\Omega_a$ are detectable on both channels.

In Fig. 6, the result after reducing the attenuator voltage to 2 V can be seen. According to Fig. 2, this increases the transmission to approx. 14%. Accordingly, the influence of the reference beam on the heterodyne signal becomes stronger and the amplitude of the high-frequency beat with the frequency Ω_3 is clearly visible in the signal waveform. In the corresponding Fast Fourier Transform additionally the frequencies Ω_1 , Ω_2 and Ω_3 appear. The distance between the frequencies Ω_2 and Ω_3 and between the frequencies Ω_3 and Ω_1 is Ω_a in each case (Eqs. 12 and 14).

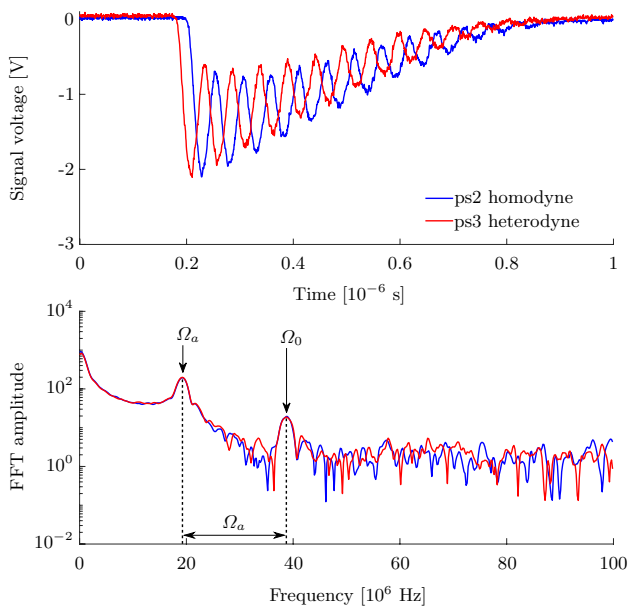


Fig. 5 Admixing the reference beam with an attenuator voltage of $U_{at} = 4$ V (see also Fig. 2), upper part: signals, lower part: corresponding Fast Fourier Transform, pulsed operation of the frequency shifter

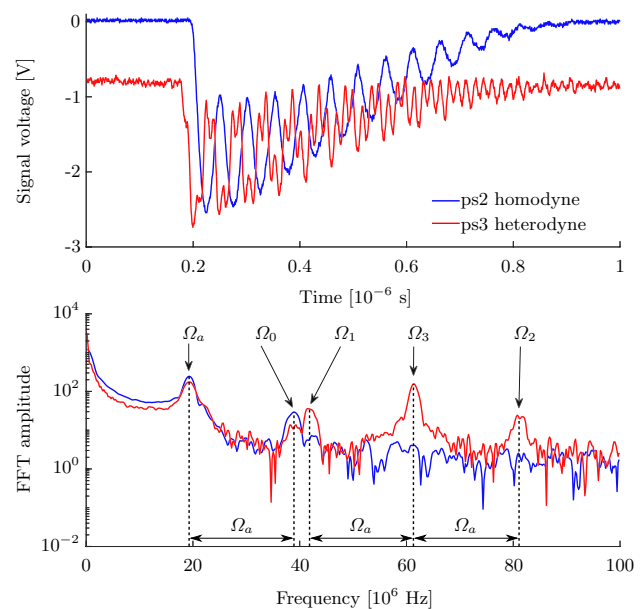


Fig. 6 Admixing of the reference beam with an attenuator voltage of $U_{at} = 2$ V (see also Fig. 2), upper part: signals, lower part: corresponding Fast Fourier Transform, pulsed operation of the frequency shifter

4.2 Single-shot experiments

Next, single-shot experiments were carried out at the shock tube of the institute using dry air as driver as well as test gas under moderate conditions, i.e. without excessive formation of NO_2 . For these measurements, seeding gas (10% NO diluted in N_2) was added in order to achieve a strong SNR. Before the experiment, the two diaphragms were inserted and the shock tube evacuated. First, the driven section was filled with seeding gas to a pressure of 20–100 mbar and then with dry air to the pressure required for the desired condition (state 1). This resulted in a NO concentration of 0.17% to 1%, depending on the condition set. The optical setup was then adjusted to achieve maximum signal strength and the grating constant was determined at room temperature.

For all test runs, the pulse energy of the pump beams was 15 mJ and the power of the probe beam 0.5 W. Depending on the signal strength, the voltage of the attenuator was set to 2.0 or 1.5 V. The voltage of the PMT was 0.75 V corresponding to a gain of approximately $2 \cdot 10^5$. The parameters of all conducted experiments in this study are summarized in Table 3.

The experiments are divided into conditions 1 to 3 according to comparable values for the measured velocity or Mach number (Table 4). Figures 7, 8 and 9 show the corresponding grouped thermometry and velocimetry data. The grouping in condition 1 to condition 3 was carried out in such a way that the measured and the calculated mean values for Mach number, velocity and temperature increase

Table 3 Experiment parameters, p_{load} refers to the pressure conditions in the tube ($p_4 - p_4/2 - p_1$), p_{seed} is the partial pressure of seeding gas (10^5 ppm NO diluted in N_2) in the driven section, *: weak reference beam intensity due to non-optimal coupler adjustment

	No.	p_{load} [bar]	p_{seed} [bar]	U_{at} [V]
Cond. 1	1	20-10-0.5	0.1	2
	2	19-10-0.5	0.1	2
	3	20-10-0.9	0.1	2
	4	20-10-0.9	0.1	2
	5	20-10-1.2	0.02	2
	6	20-10-1.2	0.02	2
	7	20-10-0.7	0.02	*0
	8	20-10-0.7	0.02	2
	9	20-10-0.7	0.02	2
	10	20-10-0.7	0.02	2
	11	20-10-0.7	0.02	2
	12	20-10-0.6	0.02	2
Cond. 2	1	19-10-0.5	0.1	2
	2	18-9-0.5	0.1	2
	3	18-9-0.2	0.02	2
	4	20-10-0.2	0.02	2
	5	20-10-0.6	0.02	2
	6	20-10-0.6	0.02	2
	7	20-9-0.6	0.02	2
	8	32-16-0.7	0.02	2
	9	35-17.5-0.7	0.02	2
	10	35-17.5-0.7	0.02	2
	11	35-17.5-0.7	0.02	2
	12	35-17.5-0.7	0.02	2
Cond. 3	1	20-10-0.2	0.02	2
	2	18-9-0.2	0.02	2
	3	20-10-0.2	0.02	2
	4	20-10-0.2	0.02	2
	5	19-9.5-0.2	0.02	2
	6	35-17.5-0.7	0.02	2
	7	35-17.5-0.5	0.02	2
	8	35-17.5-0.5	0.02	2
	9	35-17.5-0.5	0.02	1.5
	10	39-18.5-0.2	0.02	1.5
	11	30-15-0.2	0.02	1.5
	12	30-15-0.2	0.02	1.5

The experiments are grouped into condition 1–3 with comparable measured velocities/Mach numbers

Table 4 Thermometry and velocimetry using shock equations versus the evaluation of the LIGS beat frequency data (mean values \bar{x} related to each condition across all experiments)

Condition No.	Shock equations			LIGS		
	M_2	u_2 [m/s]	T_2 [K]	M_2	u_2 [m/s]	T_2 [K]
1	0.75	311	425	0.71	291	420
2	0.90	392	473	0.91	381	441
3	1.05	490	541	1.17	524	504

steadily. Note that the given values for Mach number and flow velocity describe the absolute values, i.e. the speed relative to the shock tube. It can be seen that this increase is very well reflected by both the experimentally determined and the calculated values. While the majority of the measured values are close to the respective mean values, some outliers can be seen above and below this mean value. It is noticeable that in Fig. 9 there are some clear outliers just above the mean for the measured values for Mach number but especially for velocity. These contribute to the reversal of the trend observed in Figs. 7 and 8 of lower measured than calculated values for Mach number and velocity. However, since these values should be smaller than the calculated values due to boundary layer effects, the authors suspect a low signal-to-noise ratio in these measurements as the cause for the deviations. On average, LIGS seems to measure a lower temperature in state 2, which leads to a higher measured Mach number.

LIGS is an optical measurement method that is based on the measurement of beat frequencies by superposition of a reference beam with a LIGS signal beam. Accordingly, the results refer to a measurement volume in the range of a few hundred μm and a lifetime of the laser-induced grating of up to 2 μs . The method based on the shock equations relies on measuring the velocity of the incident shock to calculate the temperature and velocity behind it. The shock velocity is determined by the transit time between two pressure sensors, and the result is therefore averaged over the volume between the sensors and the transit time (up to 200 μs). Moreover, the interaction between the shock and the boundary layer is neglected here. From these points of view, the different nature of the measurement methods implies a systematic difference in the thermometry and velocimetry data. This thesis is backed by the explicit differences displayed in Table 5. Since the LIGS method is not based on gas models and on fewer simplifications than the shock equations, the turbulent nature of the gas flow in state 2 is represented by a higher fluctuation of the LIGS results. The standard deviations σ of the measured data were calculated using Eq. 16, where x_i corresponds to the thermometry and velocimetry data, respectively, from experiment number i and \bar{x} corresponds to the mean for all N experiments. The distribution of the LIGS data around the shock equation data can be seen in Figs. 7, 8 and 9. The scatter across all experiments is described by the standard deviations of $\sigma = 0.1177$ for Mach number,

Table 5 Systematic difference between both measurement methods for thermometry and velocimetry $x_{LIGS} - x_{SE}$ (mean value and standard deviation)

	M_2	u_2 [m/s]	T_2 [K]
Mean	0.03	1	-25
σ	0.12	39	48

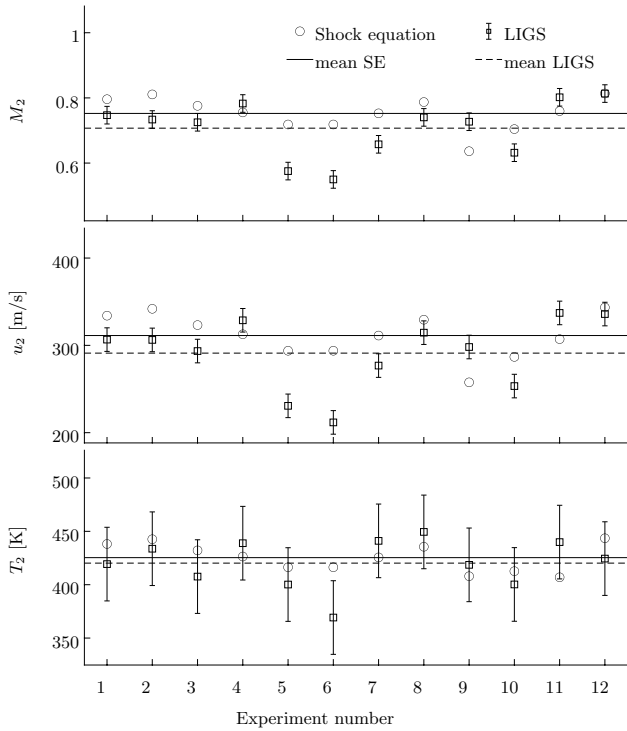


Fig. 7 Mach number, velocity and temperature behind the incident shock (state 2), LIGS measurement data in comparison to the gas dynamic shock equation results, condition 1 ($u_2 \approx 300$ m/s)

$\sigma = 39.28$ m/s for velocity and $\sigma = 48.01$ K for temperature, respectively.

$$\sigma^2 = \frac{1}{N} \sum_{i=1}^N (x_i - \bar{x})^2, \bar{x} = \frac{1}{N} \sum_{i=1}^N x_i \quad (16)$$

The measurement uncertainty of the grating constant Λ and the frequencies Ω_3 and Ω_a lead to a thermometry and velocimetry error, respectively. The propagation of the error according to the formulas in Sect. 2 was quantified by performing a Gaussian error propagation (Eq. 17) for the case of a fixed-shift resonant heterodyne LIGS.

$$\Delta x(y, z) = \sqrt{\left(\frac{\delta x}{\delta y} \cdot \Delta y\right)^2 + \left(\frac{\delta x}{\delta z} \cdot \Delta z\right)^2} \quad (17)$$

For the worst-case error propagation for the LIGS method, a reading uncertainty in the frequency spectrum of ± 0.5 MHz was assumed for Ω_3 and Ω_a . This implies an uncertainty of $\pm 0.51 \mu\text{m}$ for the grating constant Λ , leading to calculated

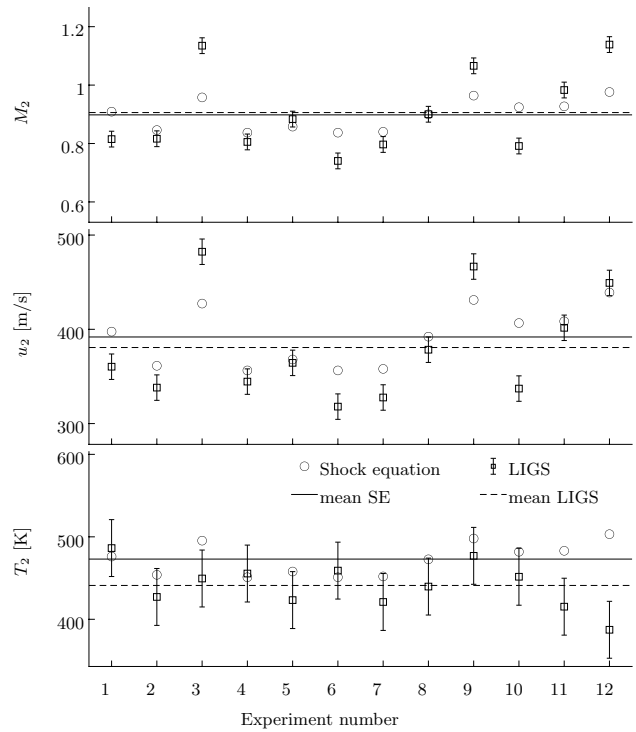


Fig. 8 Mach number, velocity and temperature behind the incident shock (state 2), LIGS measurement data in comparison to the gas dynamic shock equation results, condition 2 ($u_2 \approx 380$ m/s)

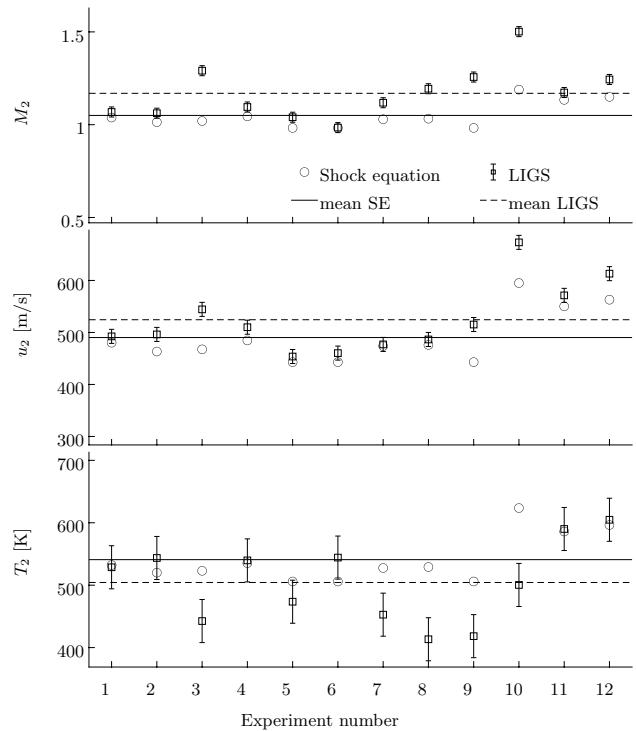


Fig. 9 Mach number, velocity and temperature behind the incident shock (state 2), LIGS measurement data in comparison to the gas dynamic shock equation results, condition 3 ($u_2 \approx 460$ m/s)

uncertainties of $\Delta_{LIGS}M_2 = \pm 0.027$, $\Delta_{LIGS}u_2 = \pm 13$ m/s and $\Delta_{LIGS}T_2 = \pm 35$ K, respectively. The estimated uncertainties of the LIGS method are displayed as error bars around the LIGS data points in Figs. 7, 8 and 9. It is important to note that the measurement of the Mach number does not depend on the grating constant (see Eqs. 3 and 11), which makes it a robust measurement in terms of error propagation and setup calibration.

Since the values for the shock equations are calculated from measured values, an estimate of the error propagation was made. Sources of error here include the diameter and placement of the pressure sensor (± 1 mm), the duration of the rising edge in the pressure signal (± 5 μ s), and a variation in the isentropic exponent due to gas temperature ($\kappa = 1.375 \pm 0.25$). For typical experimental conditions in this study, the calculated uncertainties are $\Delta_{SE}M_2 = \pm 0.12$, $\Delta_{SE}u_2 = \pm 52$ m/s, and $\Delta_{SE}T_2 = \pm 37$ K. The uncertainties calculated in this way imply that using LIGS is more accurate than using the shock equations.

5 Conclusion and outlook

Laser-induced grating spectroscopy is predestined for single-shot measurements, even at high pressures and temperatures, as it enables a high signal-to-noise ratio even under difficult measurement conditions. Thus, this measurement technique can be used on intermittently operating experimental test benches such as shock tubes and shock tunnels to measure temperatures and flow velocities.

In this work, an optical measurement setup already successfully used on a shock tunnel to measure temperatures via homodyne thermal laser-induced grating spectroscopy was extended to additionally measure flow velocities via heterodyne detection. The additional components required for this were designed for the planned application and integrated into the setup.

A second photomultiplier for the heterodyne signal allows the detection of beat frequencies of the signal beam with the reference beam and thus enables the measurement of the flow velocity. In order to clearly distinguish between the homodyne and heterodyne beat frequencies, a tunable frequency shifter was integrated into the beam path of the reference beam, shifting its frequency by the adjustable amount $\Delta\omega_s$. This increases the beat frequencies of the heterodyne signal Ω_1 , Ω_2 and Ω_3 by the amount $\Delta\omega_s$, which separates them from the beat frequencies of the homodyne signal Ω_a and Ω_0 .

Due to the simultaneous and independent detectability of the homodyne and the heterodyne signal, Ω_a and Ω_0 can be uniquely identified. In combination with the frequency shifter, this allows the detected frequencies to be unambiguously distinguished, since there are cases where the distances

between the individual beat frequencies are similar and thus they cannot be identified beyond doubt. Without the use of the frequency shifter, the ambiguity can even be so large that the frequencies overlap. This can occur, e.g., with non-shifted, non-resonant heterodyne LIGS under measurement conditions with $M \approx 1$.

This effect is amplified by a broadening of the peaks in the frequency domain, which in the worst case extends the range of ambiguity to $M = 0.8$ – 1.2 . This challenge is even greater in resonant LIGS because of the additional frequencies Ω_a and Ω_3 in the spectrum. A way to improve clarity is to ensure longer grating lifetime, since the width of the peaks in the power spectrum is inversely proportional to the corresponding signal length.

Since the frequency shifter can be controlled by a pulse synchronized with the experimental sequence, the exposure of the heterodyne photomultiplier occurs only for a short time, which prevents overexposure and significantly improves the signal-to-noise ratio. In preliminary studies, the optimal time window of 5 μ s for pulsed control of the frequency shifter was determined.

Furthermore, in this work, the reference beam and the signal beam for generating the beat frequencies were coupled into optical fibers, which contributes significantly to the stray light suppression and improves the signal quality. The attenuator, which is additionally integrated into the beam path of the reference beam, allows the intensities of the frequency-shifted reference and signal beams to be adjusted, thus maximizing the intensity of the heterodyne signal. This adjustment could be adapted to the respective optical conditions before each experiment, since the frequency shifter allows a clear distinction between homodyne and heterodyne signal without flow. It should also be mentioned that the measures described have significantly increased the success rate of the evaluable experiments.

Single-shot measurements successfully performed with this extended optical measurement setup on a shock tube under moderate conditions ($h = 0.5$ – 1.0 MJ/kg) showed beat frequencies of a thermal grating in the homodyne channel and beat frequencies from interference with the reference beam in the heterodyne channel. Evaluation of this signal in terms of heterodyne beat frequencies Ω_1 , Ω_2 and Ω_3 was possible in 36 out of 41 test runs. To analyze the measured values for Mach number, flow velocity and temperature behind the incident shock, the relationships for a normal shock were used. Here, the velocity and Mach number of the incident shock were determined from the time interval between two pressure jumps recorded by two pressure sensors installed at a distance of 50 mm from each other and the temperature of the test gas measured before the experiment.

The systematic differences in thermometry or velocimetry between the shock equations and LIGS, estimated by a priori considerations of measurement comparability,

were demonstrated with the obtained data. The estimated thermometry and velocimetry uncertainties of LIGS were calculated to be $\Delta_{LIGS}M_2 = \pm 0.027$, $\Delta_{LIGS}u_2 = \pm 13$ m/s and $\Delta_{LIGS}T_2 = \pm 35$ K, respectively, and those of the shock equations as $\Delta_{SE}M_2 = \pm 0.12$, $\Delta_{SE}u_2 = \pm 52$ m/s, and $\Delta_{SE}T_2 = \pm 37$ K.

Appendix

In the manuscript, for better readability, only the mean values of the measured data and the deviations between measured and calculated values, respectively, have been presented in Tables 4 and 5. In the appendix A, these tables are now presented in full (Table 6 and 7, respectively).

Table 6 Thermometry and velocimetry using shock equations versus the evaluation of the LIGS beat frequency data and the average values \bar{x} related to each condition

	No.	Shock equations			LIGS		
		M_2	u_2 [m/s]	T_2 [K]	M_2	u_2 [m/s]	T_2 [K]
Condition 1	1	0.80	334	438	0.75	307	419
	2	0.81	342	443	0.73	306	434
	3	0.78	323	432	0.73	293	408
	4	0.76	313	426	0.78	329	439
	5	0.72	294	416	0.58	231	400
	6	0.72	294	416	0.55	212	369
	7	0.75	311	426	0.66	277	441
	8	0.79	329	436	0.74	315	449
	9	0.64	258	408	0.73	298	419
	10	0.70	287	413	0.63	253	400
	11	0.76	307	407	0.80	337	440
	12	0.81	343	444	0.81	336	424
		Mean	0.75	311	425	0.71	291
Condition 2	1	0.91	398	476	0.82	360	486
	2	0.85	361	454	0.82	338	427
	3	0.96	427	495	1.13	482	449
	4	0.84	356	451	0.81	345	455
	5	0.86	368	458	0.88	364	423
	6	0.84	356	451	0.74	318	459
	7	0.84	358	452	0.80	328	421
	8	0.90	392	473	0.90	378	440
	9	0.96	431	498	1.07	467	477
	10	0.92	407	482	0.79	337	452
	11	0.93	408	483	0.98	402	415
	12	0.98	439	503	1.14	449	387
		Mean	0.90	392	473	0.91	381
Condition 3	1	1.04	480	532	1.07	492	529
	2	1.01	463	520	1.06	496	544
	3	1.02	468	523	1.29	544	443
	4	1.04	485	535	1.10	510	540
	5	0.98	443	506	1.04	454	474
	6	0.98	443	506	0.98	460	544
	7	1.03	474	528	1.12	477	453
	8	1.03	476	529	1.19	487	413
	9	0.98	443	506	1.26	515	418
	10	1.19	595	624	1.50	673	500
	11	1.13	550	586	1.17	571	590
	12	1.15	563	596	1.24	613	605
		Mean	1.05	490	541	1.17	524

Table 7 Systematic difference between both measurement methods for thermometry and velocimetry $x_{LIGS} - x_{SE}$ along with mean values and standard deviations

Cond. -No.	M_2	u_2 [m/s]	T_2 [K]
1-1	-0.05	-27	-19
1-2	-0.08	-36	-9
1-3	-0.05	-30	-25
1-4	0.03	16	12
1-5	-0.14	-63	-16
1-6	-0.17	-82	-47
1-7	-0.10	-34	15
1-8	-0.05	-15	14
1-9	0.09	40	11
1-10	-0.07	-33	-12
1-11	0.04	30	33
1-12	0.00	-8	-19
2-1	-0.09	-37	10
2-2	-0.03	-23	-27
2-3	0.18	55	-46
2-4	-0.03	-12	4
2-5	0.03	-4	-35
2-6	-0.10	-38	8
2-7	-0.04	-30	-31
2-8	0.00	-14	-33
2-9	0.10	35	-21
2-10	-0.13	-70	-30
2-11	0.06	-7	-68
2-12	0.16	10	-116
3-1	0.03	12	-4
3-2	0.05	33	24
3-3	0.27	77	-80
3-4	0.05	25	4
3-5	0.06	11	-32
3-6	0.00	17	38
3-7	0.09	3	-75
3-8	0.16	11	-116
3-9	0.27	72	-88
3-10	0.31	78	-123
3-11	0.04	21	4
3-12	0.09	50	8
mean	0.03	1	-25
σ	0.12	39	48

Funding Open Access funding enabled and organized by Projekt DEAL.

Open Access This article is licensed under a Creative Commons Attribution 4.0 International License, which permits use, sharing, adaptation, distribution and reproduction in any medium or format, as long as you give appropriate credit to the original author(s) and the source, provide a link to the Creative Commons licence, and indicate if changes were made. The images or other third party material in this article are included in the article's Creative Commons licence, unless indicated otherwise in a credit line to the material. If material is not included in the article's Creative Commons licence and your intended use is not

permitted by statutory regulation or exceeds the permitted use, you will need to obtain permission directly from the copyright holder. To view a copy of this licence, visit <http://creativecommons.org/licenses/by/4.0/>.

References

1. K. Schemperg, Ch. Mundt, *Study of numerical simulations for optimized operation of the free piston shock tunnel HELM, 15th AIAA International Space Planes and Hypersonic Systems and Technologies Conference, AIAA-2008-2653* (Dayton, OH, USA, 2008)
2. Ch. Mundt, Development of the New Piston-Driven Shock-Tunnel HELM, in: O. Igra, F. Seiler (eds.) *Experimental Methods of Shock Wave Research*, Volume 9 of the series *Shock Wave Science and Technology Reference Library* pp. 265-283, (Springer Verlag, 2015)
3. T. Sander, P. Altenhöfer, Ch. Mundt, Development of laser-induced grating spectroscopy for application in shock tunnels. *J Thermophys Heat Transf* **28**(1), 27–31 (2014). <https://doi.org/10.2514/1.T4131>
4. B. Williams, M. Edwards, R. Stone, J. Williams, P. Ewart, High precision in-cylinder gas thermometry using Laser Induced Gratings: quantitative measurement of evaporative cooling with gasoline/alcohol blends in a GDI optical engine. *Combustion and Flame* **161**(1), 270–279 (2014). <https://doi.org/10.1016/j.combustflame.2013.07.018>
5. T. Mizukaki, T. Matsuzawa, Application of laser-induced thermal acoustics in air to measurement of shock-induced temperature changes. *Shock Waves* **19**(5), 361–369 (2009). <https://doi.org/10.1007/s00193-009-0218-6>
6. J.P. Kuehner, F.A. Tessier, A. Kisoma, J.G. Flittner, M.R. McErlean, Measurements of mean and fluctuating temperature in an underexpanded jet using electrostrictive laser-induced gratings. *Experiments in Fluids* **48**(3), 421–430 (2010). <https://doi.org/10.1007/s00348-009-0746-y>
7. F. J. Förster, S. Baab, G. Lamanna, B. Weigand, Temperature and velocity determination of shock-heated flows with non-resonant heterodyne laser-induced thermal acoustics, *Applied Physics B*, Vol. 121, No. 3, 1 Sep. 2015, pp. 235-248, <https://doi.org/10.1007/s00340-015-6217-7>
8. S. Schlamp, T. Rösgen, D.N. Kozlov, C. Rakut, P. Kasal, J. von Wolfersdorf, Transient grating spectroscopy in a hot turbulent compressible free jet. *J Propulsion Power* **21**(6), 1008–1018 (2005). <https://doi.org/10.2514/1.13794>
9. P.M. Danehy, P.H. Paul, R.L. Farrow, Thermal-grating contributions to degenerate four-wave mixing in nitric oxide. *J Opt Soc Am B* **12**(9), 1564–1576 (1995). <https://doi.org/10.1364/JOSAB.12.001564>
10. S. Schlamp, T.H. Sobota, Measuring concentrations with laser-induced thermalization and electrostriction gratings. *Exp Fluids* **32**(6), 683–688 (2002). <https://doi.org/10.1007/s00348-002-0419-6>
11. E. B. Cummings, Laser-induced thermal acoustics: simple accurate gas measurements, *Optics Letters*, Vol. 19, No. 17, 1 Sep. 1994, pp. 1361-1363, <https://doi.org/10.1364/OL.19.001361>
12. D.J.W. Walker, R.B. Williams, P. Ewart, Thermal grating velocimetry. *Opt. Lett.* **23**(16), 1316–1318 (1998). <https://doi.org/10.1364/OL.23.001316>
13. D.N. Kozlov, Simultaneous characterization of flow velocity and temperature fields in a gas jet by use of electrostrictive laser-induced gratings. *Appl. Phys. B* **80**, 377–387 (2005). <https://doi.org/10.1007/s00340-004-1720-2>
14. D.N. Kozlov, J. Kiefer, T. Seeger, A.P. Fröba, A. Leipertz, Simultaneous measurement of speed of sound, thermal diffusivity, and

- bulk viscosity of 1-ethyl-3-methylimidazolium-based ionic liquids using laser-induced gratings. *J. Phys. Chem. B* **118**, 14493–14501 (2014). <https://doi.org/10.1021/jp510186x>
15. S. Schlamp, E.B. Cummings, T.H. Sobota, Laser-induced thermal-acoustic velocimetry with heterodyne detection. *Opt. Lett.* **25**(4), 224–226 (2000). <https://doi.org/10.1364/OL.25.000224>
 16. S. Schlamp, E. Allen-Bradley, *Homodyne detection laser-induced thermal acoustics velocimetry, 38th Aerospace Sciences Meeting & Exhibit, AIAA-2000-0376* (Reno, NV, USA, 2000)
 17. B. Hemmerling, M. Neracher, D.N. Kozlov, W. Kwan, R. Stark, D. Klimenko, W. Clauss, M. Oswald, Rocket nozzle cold-gas flow velocity measurements using laser-induced gratings. *J. Raman Spectrosc.* **33**, 912–918 (2002). <https://doi.org/10.1002/jrs.946>
 18. M. Neracher, W. Hubschmid, Heterodyne-detected electrostrictive laser-induced gratings for gas-flow diagnostics. *Appl. Phys. B* **79**, 783–791 (2004). <https://doi.org/10.1007/s00340-004-1632-1>
 19. S. Baab, F.J. Förster, G. Lamanna, B. Weigand, Speed of sound measurements and mixing characterization of underexpanded fuel jets with supercritical reservoir condition using laser-induced thermal acoustics. *Exp. Fluids* **57**(11), 172–184 (2016). <https://doi.org/10.1007/s00348-016-2252-3>
 20. E. B. Cummings, I. A. Leyva, H. G. Hornung, Laser-induced thermal acoustics (LITA) signals from finite beams, *Applied Optics*, Vol. 34, No. 18, 20 Jun. 1995, pp. 3290-3302, <https://doi.org/10.1364/AO.34.003290>
 21. A. Stampanoni-Panariello, D. N. Kozlov, P. P. Radi, B. Hemmerling, Gas phase diagnostics by laser-induced gratings I. Theory, *Applied Physics B*, Vol. 81, Issue 1, 3 Jun. 2005, pp. 101-111, <https://doi.org/10.1007/s00340-005-1852-z>
 22. A. Stampanoni-Panariello, D.N. Kozlov, P.P. Radi, B. Hemmerling, Gas phase diagnostics by laser-induced gratings II. *Exp. Appl. Phys. B* **81**, 113–129 (2005). <https://doi.org/10.1007/s00340-005-1853-y>
 23. P. Altenhöfer, T. Sander, Ch. Mundt, *Preliminary Experiments for Temperature Measurements in Shock Tunnels Using Laser-Induced Electrostrictive Gratings, 17th International Space Planes and Hypersonic Systems and Technologies Conference, AIAA-2011-2211* (CA, USA, San Francisco, 2011)
 24. T. Sander, P. Altenhöfer, Ch. Mundt, Temperature Measurements in a Shock Tube using Laser-Induced Thermal Grating Spectroscopy, *Proceedings of the 17th International Conference on the Methods of Aerophysical Research (ICMAR)*, Vol. 1, Jul. 2014, pp. 178-179, Novosibirsk, Russia
 25. T. Sander, P. Altenhöfer, Ch. Mundt, Temperature Measurements in a Shock Tube Using Laser-Induced Grating Spectroscopy. *J. Thermophys. Heat Transf.* **30**(1), 62–66 (2016). <https://doi.org/10.2514/1.T4556>
 26. C. Selcan, T. Sander, P. Altenhöfer, F. Koroll, Ch. Mundt, Stagnation Temperature Measurements in a Shock-Tunnel Facility Using Laser-Induced Grating Spectroscopy. *J. Thermophys. Heat Transf.* **32**(1), 226–236 (2018). <https://doi.org/10.2514/1.T5199>
 27. P. Altenhöfer, T. Sander, F. Koroll, Ch. Mundt, LIGS Measurements in the Nozzle Reservoir of a Free-Piston Shock Tunnel. *Shock Waves* (2018). <https://doi.org/10.1007/s00193-018-0808-2>
 28. C. Selcan, T. Sander, Ch. Mundt, In situ nozzle reservoir thermometry by laser-induced grating spectroscopy in the HELM free-piston reflected shock tunnel. *Shock Waves* (2020). <https://doi.org/10.1007/s00193-020-00982-9>
 29. R.W.B. Pearse, A.G. Gaydon, *The Identification of Molecular Spectra*, 4th edn. (Chapman and Hall, London, 1976)
 30. D. K. Hsu, D. L. Monts, R. N. Zare, *Spectral Atlas of Nitrogen Dioxide 5530-6480 Ångström*, (Academic Press, New York, ISBN 0-12-357950-3
 31. T. Sander, P. Altenhöfer, L. Kleiner, Ch. Mundt, Investigation of NO₂ Absorption Behaviour around 593 nm for Seeding Purposes. *Int. J. Eng. Res. Appl. (IJERA)* **9**(8), 4–11 (2019). <https://doi.org/10.9790/9622-0908030411>

Publisher's Note Springer Nature remains neutral with regard to jurisdictional claims in published maps and institutional affiliations.